Electro-Mechanical Characteristics of Dual-Winding Motor According to Winding Arrangement for Brake Systems in Highly Automated Driving Vehicles

Baik-Kee Song, Jae-Hyun Kim, Kyu-Yun Hwang, *Member, IEEE*, and Myung-Seop Lim, *Member, IEEE*

***Abstract*—Manufactures of automotive parts are struggling to secure redundancy in various ways. An alternative is to configure the system via a dual-winding motor and two electronic control units (ECUs). The dual-winding motor contains different winding arrangements according to poles/slots, and when only one of the two circuits is used owing to a failure, the electrical and mechanical characteristics differ depending on the winding arrangement. In this study, the electrical and mechanical characteristics were analyzed and compared according to the winding arrangement when the failure occurs. In particular, the winding arrangement of the motor is divided into line symmetry, point symmetry, and alternating symmetry. For each winding arrangement, the back-electromotive force, torque, and torque ripple were compared and analyzed through simulation and test. Also, vibration caused by electromagnetic force was analyzed. Here, to consider the tooth modulation effect, concentrated force was investigated and tangential force as well as radial force were considered. Additionally, the thermal characteristics were analyzed during fault operation using a lumped parameter thermal network with piecewise stator-housing modules. Lastly, the mechanical design characteristics of the motor hardware size that need to be changed according to the winding arrangement of the brake motor are explained. This study provides guidelines for the winding arrangement selection of a dual-winding motor with a similar magnetic field distribution suitable for the design purpose, by analyzing the electromechanical characteristics and size according to the winding arrangement during fault operation. The characteristics of other motor types or pole and slot number combinations can also be inferred from the results of this study, since the magnetic flux density distribution will be determined with line, point and alternating symmetry.**

***Index Terms*—Brake system, deformation, dual-winding motor, electromagnetic force, fault-tolerant motor, highly autonomous driving (HAD), integrated electronic brake (IEB), lumped parameter thermal network (LPTN), thermal, torque ripple, winding arrangement.**

Manuscript received 11 January 2022; revised 31 May 2022 and 28 September 2022; accepted 29 April 2023. Date of publication 3 May 2023; date of current version 17 October 2023. This work was supported by the National Research Foundation of Korea (NRF) grant funded by the Korea government (MSIT) under Grant RS-2023-00207865. The review of this article was coordinated by Dr. Wei Xu. *(Correspondng author: Myung-Seop Lim.)*

Baik-Kee Song, Jae-Hyun Kim, and Myung-Seop Lim are with the Department of Automotive Engineering, Hanyang University, Seoul 04763, South Korea (e-mail: songbk82@gmail.com; zerg1258@hanyang.ac.kr; myungseop@hanyang.ac.kr).

Kyu-Yun Hwang is with the School of Railway Operation and Control, Dongyang University, Yeongju-si 36040, South Korea (e-mail: kyhwang@dyu.ac.kr).

Digital Object Identifier 10.1109/TVT.2023.3272729

I. Introduction

THERE are two main keywords defining the future automotive industry: eco-friendly and autonomous driving vehicles. The paradigm of the automotive industry is rapidly changing from internal combustion engines (ICEs)–self driving to electric powered–autonomous driving because of the influence of automation, connectivity and artificial intelligence (AI), leading to the convergence of advanced technology. From the perspective of eco-friendly automobiles, as social interest in environmental conservation and energy sustainability increases, many countries are increasingly reinforcing environmental regulations related to automobile exhaust gases. From the perspective of highly autonomous driving (HAD) vehicles, HAD frees drivers physically and mentally; thus, it offers a paradigm that transforms simple means of transportation into a smart private office with abundant infotainment. In addition to improving the quality of life, the reaction time of an improved autonomous driving system is faster than that of humans, so the number of traffic collisions can be greatly reduced.

It is important to develop traction motors, self-driving algorithms, software, and databases to facilitate for the eco-friendly and autonomous driving. However, brake systems responsible for safety, such as decelerating, stopping and maintaining in moving vehicles, are more important. Accordingly, it is necessary to study a brake motor that plays a critical role in converting a mechanical-hydraulic pressure brake to an electrical-hydraulic pressure brake according to a change in the drivetrain. In particular, in HAD, the fallback system, which is performed by humans in the conventional system, must be implemented by the motor. Therefore, it is necessary to study the motor design and motor characteristics that reflect fault-tolerant (redundancy) characteristics necessary for the brake system in HAD. Numerous studies have been conducted on fault-tolerant motors, which are the main power source of each component for fault-tolerant systems in autonomous vehicles. The research on fault-tolerant motors is primarily divided into topology and fault characteristics.

Regarding the study on the magnetic coupling and topology of dual-winding motor, which is a type of fault tolerant motor, C. Jeong suggested a winding function theory to calculate the inductance for torque calculation of a dual three-phase synchronous reluctance motor, and the torque calculated using the suggested method was verified by comparing the test results [1]. However, the motor characteristics under the fault condition were not analyzed. In [2], X. Cui studied

the electrical characteristics of the magnetic polarity change according to the winding method of a dual-channel switched reluctance machine. H. Chen studied the magnetic-coupling characteristics of a five-phase dual-rotor PMSM with one stator as an alternative to a fault-tolerant PMSM based on magnetic circuit and finite-element methods [3]. For both studies, the electrical characteristics such as torque of the machine were investigated under the channel fault condition, but multi-physics characteristics, such as thermal, noise and vibration performance were not analyzed. E. Mese compared the motor characteristics of the distributed and concentrated winding topologies of a dual winding permanent magnet synchronous machine (PMSM) [4]. T. Shigeta generalized the fundamental principle of the dual-winding method to solve the problem of high terminal voltage value and torque ripple in a compound magneto-motive force motor with two magnet properties [5]. However, the motor performance under fault conditions is not addressed in these studies. In [6], C. Babetto explained the characteristics related to torque, torque ripple, radial force, and magnetic coupling based on the winding arrangement of a synchronous reluctance motor with dual three-phase winding which comprised an 8-pole 72-slot distributed winding. The torque ripple and radial force were analyzed under faulty condition, but considerations in thermal characteristics were not investigated. A. M. EL-Refaie and W. Zhao reviewed the topology and design of modern permanent magnet (PM)-based fault-tolerant machines [7], [8]. Moreover, Y. Demir proposed a novel asymmetric stator winding in a six-phase PM synchronous motor [9].

Furthermore, studies on the characteristics of the motor failure mode have been conducted in fault-tolerant motors. Nicola [10] found a correlation between the braking torque and motor parameters under a short-circuit fault in two motors on the same shaft for a redundant solution, and optimized the motor via this relationship. However, this study focuses on the introduction of the two-motor topology for fault tolerant system rather than the analysis of the motor characteristics in the fault operation. In [11], average torque, torque ripple and unbalanced radial force in faulty operating conditions were analyzed according to the winding arrangement. However, only unbalanced radial forces were dealt, and other low-order spatial harmonic electromagnetic forces were not discussed. M. Barcaro investigated the thermal characteristics of dual three-phase 12-slot 10-pole machine under inverter faulty condition [12]. However, thermal analysis was not analyzed according to the winding arrangement. Since the electromagnetic losses and thermal conduction and convection characteristics vary greatly depending on the winding arrangement, the temperature of the motor must be considered according to the winding arrangement.

M. Chowdhury analyzed the torque and torque ripple for double-wound single and double repetition windings under winding fault scenarios [13]. P.S. Sangha analyzed the performance of a dual-winding PM motor under faults at machine terminals using FEA, and the results were compared with test measurements [14]. Similarly, J. Xu investigated the effect of fault modes on post-fault performance, such as open or short circuits, in a permanent magnet (PM) synchronous motor. However, these studies have limitations in that there is no analysis according to the winding arrangement, and only the torque were investigated. Yao investigated the fault-tolerant performance of a doubly-salient brushless DC generator [15], [16]. P. Giangrande suggested a post-fault control strategy for balancing the braking torque by considering short-circuit faults and confirmed its feasibility via thermal analysis [17]. S.J. Nall studied the electrical and thermal behavior of four separate three-phase PM machines for normal and fault scenarios [18]. All the above studies were conducted without considering 2-3 of the various characteristics that must be considered when designing a motor. Also, although the winding arrangement greatly affects the performance of the motor in the event of a fault, this has not been taken into account.

As reviewed above, electromagnetic studies on motor topology and motor performance under fault conditions are actively being conducted. However, there are more factors to consider when designing a motor product, not only electromagnetic design; factors include electromagnetic-, noise and vibration-, thermal- and mechanical- design characteristics. These design factors come together to make a motor product. However, there are few comprehensive comparative studies on fault-tolerant motors, such as electromagnetic, noise and vibration, thermal and size characteristics based on the winding arrangement, that can serve as guidelines for engineers. In addition, although the multi-physics characteristics in fault conditions are greatly affected according to the winding arrangement, such studies have not been conducted much. This paper has the advantage of suggesting a direction for a motor product design by analyzing the advantages and disadvantages of each design factor and their reasons; for example, it has advantage in selecting winding arrangements by prioritizing electrical-, noise and vibration-, thermal-, and mechanical design characteristics when designing products for dual winding motors. This comparative study allows engineers to select appropriate winding arrangements when designing or selecting a fault-tolerant motor suitable for application depending on the critical design purpose.

This paper is organized as follows. In Section II, the operating principle and system configuration of the conventional brake system (CBS) and integrated electronic brake (IEB) are explained, and importance of dual-winding motor of IEB in HAD are introduced. In Section III, three winding arrangements of the dual-winding motor are presented for characteristic comparison during fault operation. According to the winding arrangements, electric characteristics such as back electromotive force (EMF) and torque, noise and vibration characteristics such as radial, tangential force and deformation considering tooth modulation effect, thermal, and price and size characteristics are analyzed in detail. Finally, in Section IV, the comparison results are summarized, and conclusion is drawn.

II. Brake System for HAD Vehicles

Since the control system drives instead of a person in autonomous vehicles, the brakes must cope with emergency situations as an active type rather than a conventional passive type. In this role, the IEB is effective because it activates the brake as an electrical signal. In HAD, because humans are not involved in driving, a redundant brake system is required that can perform the same function in the case of brake failure.

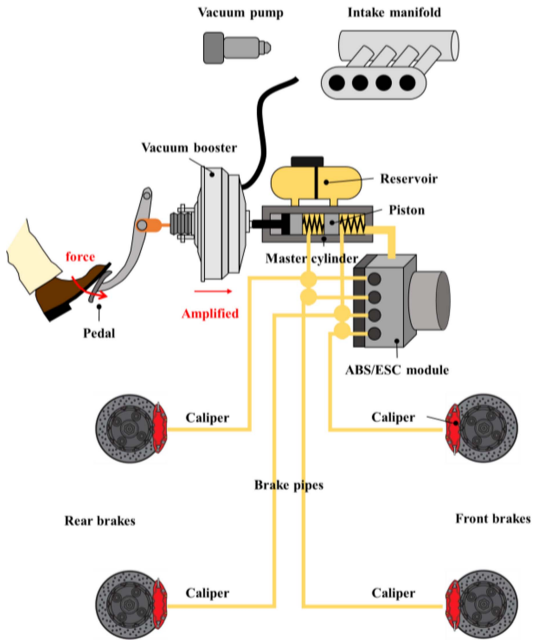

Fig. 1. Conventional brake system having an antilock brake system (ABS) with electronic stability control (ESC).

Occasionally, brake manufacturers include two brake systems within vehicles, and as an alternative, they configure a redundant system using two ECUs and a dual-winding motor for the redundant system. In a redundant system that utilizes a dual-winding motor, the motor should be designed considering both normal and fault operating condition. Even if one circuit fails and only operates with other circuit in a fallback situation, the pressure in the caliper required to stop the vehicle is the same in normal operation. This means that the same torque is required in the fault operation. Therefore, it is necessary to consider fault operating characteristics when designing the dual-winding motor of the brake redundant system. Since the electrical, mechanical, thermal, and price and size characteristics are changed according to the winding arrangement in the dual-winding motor during fault operation, it is important to understand the characteristics that should be selected for the design. Therefore, this paper investigates the characteristics according to the winding arrangement in the dual-winding motor that is used for IEBs.

A. System Configuration

As shown in Fig. 1, in CBS, the brake system is primarily composed of five subsystems. The subsystems include a vacuum booster, master cylinder, anti-lock brake system (ABS) /electronic stability control (ESC) module, brake pipes and calipers. The operation sequence of CBS is as follows: In CBS, the energy source comprises muscular pedal efforts applied by the driver, combined with a vacuum booster. The vacuum booster amplifies the foot pressure generated when the brake pedal is depressed. Consequently, it reduces the manual effort required for the actuation. In the event of a boost fault, the driver can still apply the brakes using muscular effort alone [19]. When the brake pedal is depressed, the driver's effort is instantly transmitted to

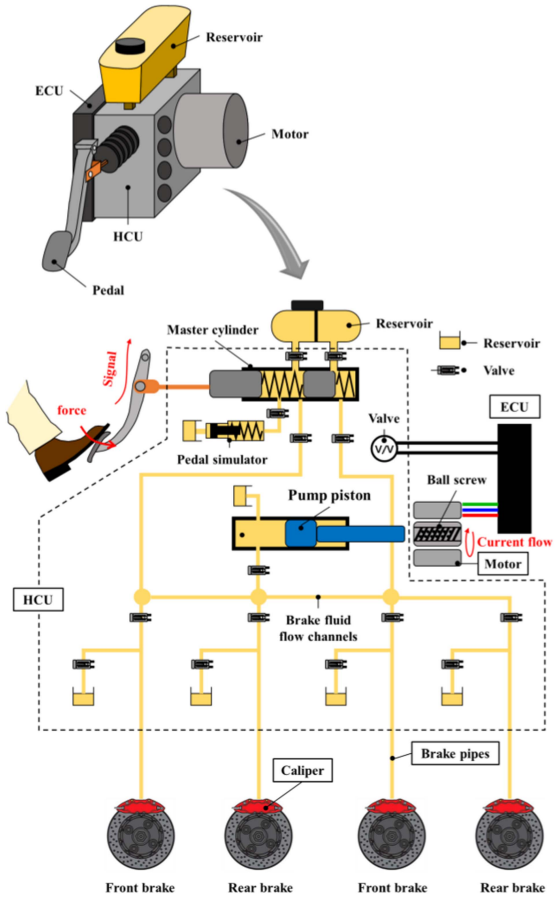

Fig. 2. Integrated electronic brake system.

the brake fluid in the master cylinder through the piston of the master cylinder. According to Pascal's principle, the pressure is transmitted to each wheel cylinder via the brake pipe and caliper piston. The pressure transferred to the caliper piston is converted into a compressive force acting on the brake pads.

The IEB replaces the vacuum booster in the CBS by directly actuating the pump piston using the motor to generate the braking pressure, which includes all functions of the ESC/ABS in one module. Fig. 2 illustrates the IEB layout and internal structure. The IEB comprises an electronic control unit (ECU), hydraulic control unit (HCU), motor, brake pipe, and caliper. As shown in Fig. 2, the HCU comprises a master cylinder, motor and ball screw, pump, piston, pedal simulator, and many valves. The master cylinder operates the brake with human force in case of a system fault. It has the same role as the master cylinder in a conventional brake. During normal operation without fault, the motor generates torque to apply force to the piston. Accordingly, the ball screw converts the rotational torque of the motor to a linear force. Subsequently, the piston receives force from the motor and gear and pushes the brake fluid in the pump to generate the braking pressure. During normal operation, the motor generates the braking pressure; therefore, the driver's pedal force is not required. As depicted in Fig. 2, the IEB is lighter because it has fewer parts compared to the CBS, and it generates braking pressure using the motor instead of the vacuum booster, which requires vacuum from the intake manifold or vacuum pump;

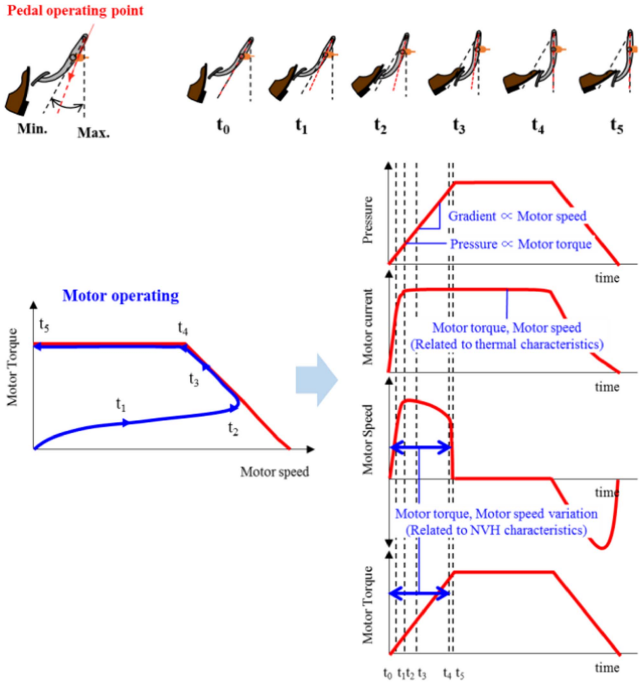

Fig. 3. Motor characteristics during AEB of IEB operation.

thus, it is not only eco-friendly but also effective in improving fuel efficiency.

B. Motor Characteristics in IEB Operation

During the IEB operation, the motor operation is dependent on increasing the pressure of the brake caliper. For example, Fig. 3 illustrates the motor current, speed, and torque according to the time and pressure during autonomous emergency braking (AEB), and shows pedal input at that time. The slope of the caliper pressure according to motor differs depending on the vehicle's caliper characteristics and pressure range, but in general, the slope of the wheel pressure is related to the motor speed. In addition, the magnitude of the pressure is proportional to the motor torque, which is related to electrical characteristics. In an AEB, the maximum output of the motor is required to increase the response performance of the brake, and thus, the maximum current of the motor is applied. Even when the pressure is kept constant, the current is kept constant because the torque of the motor is constant. Therefore, the motor is always operating when the brake is operating, and the current is continuously applied during operation, so the thermal characteristics of the motor that determine the operation time of the motor is one of the significant design factors. Fig. 4 illustrates a graph of the caliper pressure and sound amplitude obtained in a vehicle experiment. When the motor operates from t_1 to t_5 (Fig. 3), an operating sound is generated. The sound is generated from the electromagnetic force and torque ripple of the motor, and gear noise by motor rotation and speed changes when the pressure increases. In a CBS, the motor is not used during brake operation, and the operating sound is very small. However, the operating sound in an IEB is larger than that in the CBS, and is inevitable. Therefore, because this noise is unfamiliar to the driver, it may cause a

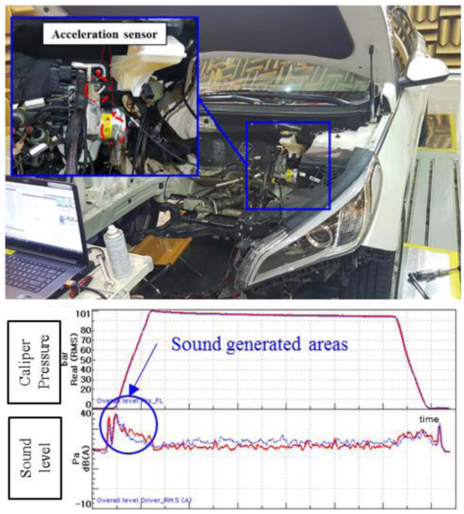

Fig. 4. Operating sound in vehicle test.

sense of heterogeneity. In this aspect, the noise and vibration characteristics owing to the electromagnetic force and torque ripple of the motor are critical.

C. Dual-Winding Motor of IEB for HAD

In this section, a fault tolerant IEB system using a dual-winding motor in consideration of HAD is described. As mentioned earlier, the IEB is suitable for HAD because braking pressure is unrelated to human pedal inputs. The pump piston, which generates the braking pressure, is connected to the motor that operates only by signals transmitted to the ECU. Therefore, only an electrical signal is required during HAD to generate the required braking pressure.

In safety-conscious chassis products such as steering and braking systems, fault-tolerant systems are configured to allow the driver to manually use minimum performance during a fault. However, if a system failure occurs in an emergency situation during HAD, the driver is not driving and may not be able to respond quickly to the situation. Therefore, an additional fault-tolerant system that does not require the driver's input is required to cope with the aforementioned situation, even in the case of a system fault during HAD. Similarly, in the brake system for HAD, a fault-tolerant motor and ECU are required as countermeasures against faults. Therefore, in the fault-tolerant brake system covered in this study, the circuit of the motor is divided into two circuits, and the ECU is separated into two for controlling the motor, as shown in Fig. 5. Only the electrical components, the motor and controller consist of two systems because the mechanical parts are assumed to be sufficiently robust and reliable. The primary and secondary controllers of the IEB ECU receive traffic conditions from various sensors of the vehicle and calculate the braking pressure appropriate for the driving situation. Primary and secondary controllers of the IEB's ECU input the corresponding motor current into the primary and secondary circuits of the motor to make the motor torque suitable for the required braking pressure. The primary and secondary motor circuits are controlled in phases, with each

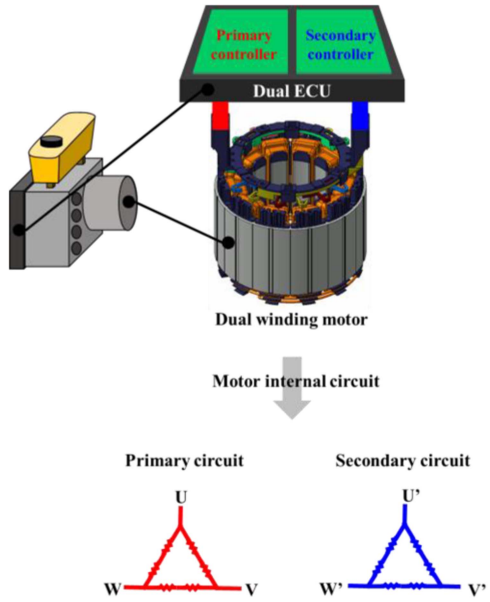

Fig. 5. Dual-winding motor and a ECU of IEB considering HAD.

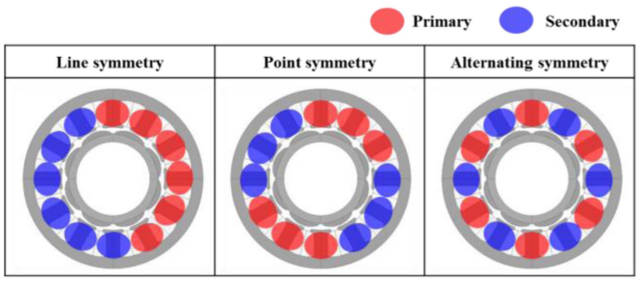

Fig. 6. Winding arrangement of 8-pole 12-slot dual-winding motor.

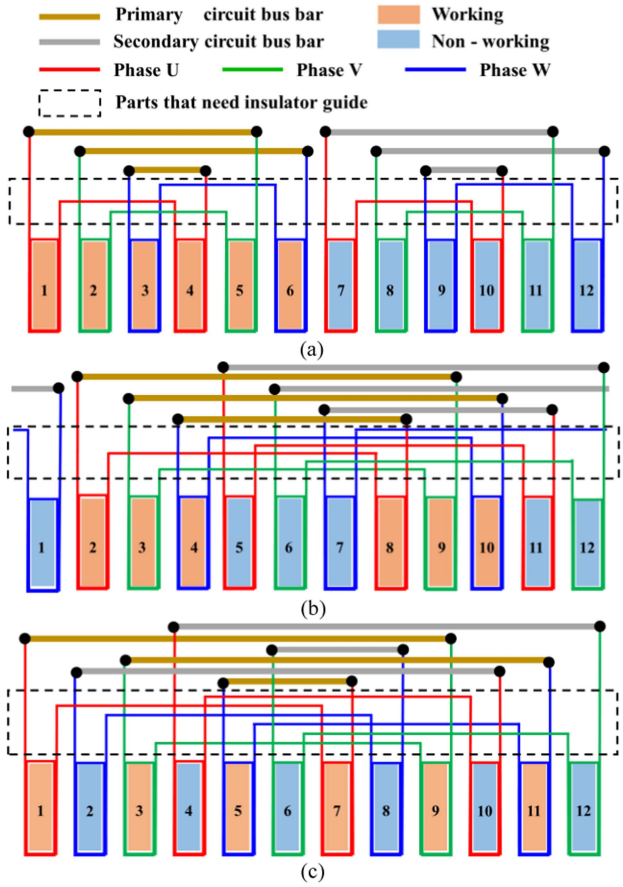

Fig. 7. Bus-bar and winding connection according to winding arrangement. (a) Line symmetry. (b) Point symmetry. (c) Alternating symmetry.

phase generating half of the required torque. The combined torque of each circuit moves the pump piston and produces braking pressure. However, the IEB operates during faults in the HAD as follows: We assume that the primary controller of the IEB ECU fails. Only the secondary controller of the IEB drives the secondary circuit of the motor. Even when only one circuit is operated owing to failure, the motor is required to ensure system performance. During fault operation, twice as much current is applied to the secondary circuit of the motor to generate the same braking as in normal operation, in contrast to the case during normal operation. Consequently, in the IEB, the motor should be designed according to specific criteria that prevent problems, even if it continuously operates in the mainly used operating points during fault operation.

III. Dual-Winding Motor Characteristics

There are three methods of winding arrangement, as shown in Figs. 6 and 7; the winding connection correspond to the winding arrangement. Table I lists the specifications of the dual-winding motor. Under the normal operation (without fault), the performance of three winding arrangements is exactly the same. However, the winding arrangement of a dual-winding motor affects thermal, noise, vibration, and electrical characteristics. The overall price and size are also affected by winding arrangements.

TABLE I
Dual-Winding Motor Specifications for Fault-Tolerant IEB

Items	Value	Remark
Motor type	SPMSM	
Winding type	Concentrated	
Winding connection	Delta	
Pole / slot	8 / 12	
Max. torque (Nm)	3.3	@ 50 A_{pk}, each terminal

A. Electric Characteristics

For the electrical characteristics, the measured torque and torque ripple with the fabricated motor were compared with the simulation results.

1) No-Load Characteristics: Before the load test, the back EMF at no-load was compared with the simulation and test results. Since there is no current input, the no-load back EMF is the same regardless of the winding arrangement. Fig. 8 illustrates the back EMF waveform and the amplitude of the fundamental and harmonic components of the back EMF through fast Fourier transform (FFT). The amplitude of the fundamental component

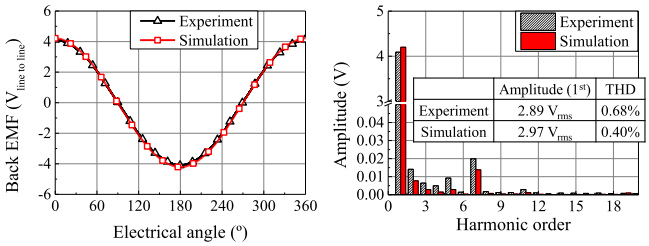

Fig. 8. No-load characteristics (back-EMF).

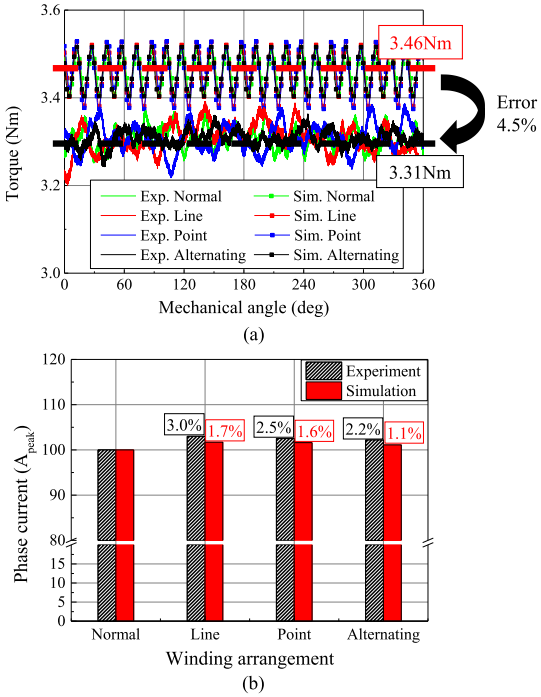

Fig. 9. Load characteristics (torque and phase current). (a) Torque and torque ripple. (b) Phase current for same output torque.

of the back EMF was 2.89 V_{rms} and 2.97 V_{rms} in the test and simulation, respectively, with an error of approximately 2.84%. This error was primarily caused by the tolerance of the permanent magnet, stator, and rotor core, and the smaller the motor, the more sensitive it is. The total harmonic distortion (THD) of the back EMF is 0.68% and 0.4% of the test value and simulation value, respectively, which is close to the design value.

2) Load Characteristics: After measuring the motor torque based on 100 A_{pk} (primary: 50 A_{pk}, secondary: 50 A_{pk}) in the normal operation, the amplitude of the current was changed to generate the same torque even in the fault operation to measure the torque ripple under the same load. The torque error of the simulation and test was approximately 4.5%, and the increase in current to generate the same torque in the case of fault operation was 2% for the simulation and approximately 2∼3% for the test as shown in Fig. 9. The current increment is large in the order of line > point > alternating in symmetry, which originates from the difference in reluctance of the magnetic circuit at the load, showing the same trend in the tests and simulations. However, the current increment is very small and within an error level.

TABLE II
TORQUE HARMONICS

SYMMETRY	EXPERIMENT	SIMULATION
Normal	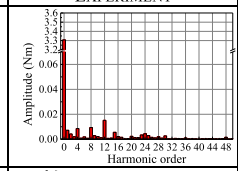	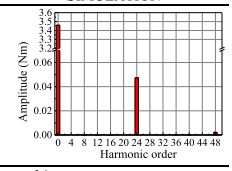
Line	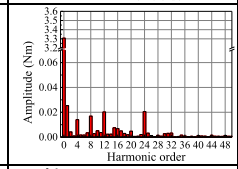	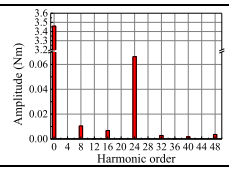
Point	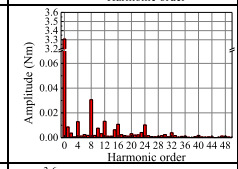	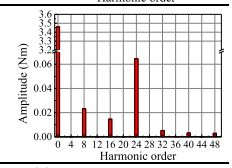
Alternating	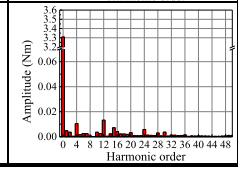	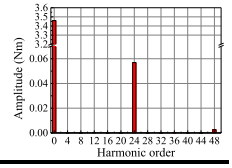

Besides, the magnitude of the torque according to the winding arrangement is similar. However, it is necessary to analyze the harmonic order component of torque due to noise caused by torque ripple. Table II lists the torque harmonics generated during one rotation of the rotor, which was calculated through FFT analysis. In the simulation results, the torque harmonics of multiples of the 8th order in addition to the 24th order appeared in line symmetry and point symmetry. However, it did not occur in alternating symmetry. In the simulation, the 24th component is the largest. However, there are orders larger than the 24th component in the test value, which is primarily due to assembly tolerance and dimensional tolerance caused by manufacturing, and is inevitable. As shown in Fig. 10, the torque multiples of the 8th order which is generated in simulation with ideal condition were compared to confirm the similarity between the test result and the simulation result. Although there is a difference in the values, the simulation and test results were similar tendency. From the results, alternating symmetry is judged to be advantageous in all orders of torque ripple [20], and line and point symmetries have different advantages depending on the order. The results demonstrate that alternating symmetry is conducive for noise and vibration.

B. Noise and Vibration Characteristics

The factors affecting noise and vibration include deformation by electromagnetic force and torque ripple by the motor shaft. Instead of measuring noise and vibration, deformation analysis of the dual-winding motor based on the winding arrangement during fault operation was performed via finite element analysis (FEA). Here, in order to consider the tooth modulation effect,

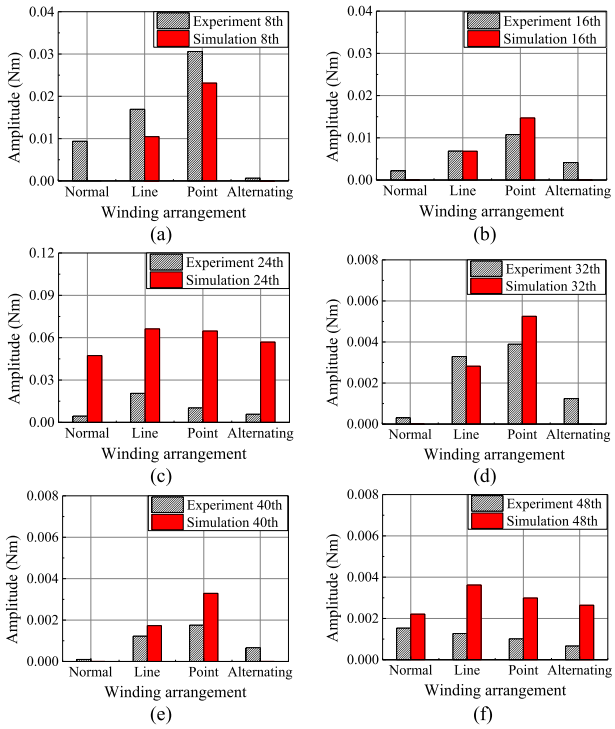

Fig. 10. 8X harmonics of torque ripple. (a) 8th order. (b) 16th order. (c) 24th order. (d) 32th order. (e) 40th order. (f) 48th order.

when analyzing the electromagnetic force, concentrated force was calculated and compared instead of distributed force.

1) Basic Theory of Spatial Harmonics and Vibration Order: The spatial harmonic orders of the magneto-motive force (MMF) of the armature's and field's based on the pole and slot combinations are discussed. The vibration order is calculated via the combination of the spatial harmonic order of the armature's and field's MMF. The deflection Δd of the stator core is an inverse function of the fourth power of the force order r when only the pure circumferential vibration orders of the stator core are considered [21].

$$\Delta d \propto \frac{1}{r^4} \tag{1}$$

Therefore, the smaller the vibration order, the greater the amount of deformation, which is unfavorable for vibration and noise. The vibration order is determined from the combination of the spatial harmonics orders of the armature's and field's MMF.

The spatial harmonic orders of the armature's MMF are obtained using (3) and (4) depending on whether the value of n obtained by using the number of slots per pole phase in (2) is odd or even. The number of slots per pole is

$$q_1 = \frac{s_1}{2\text{mp}} = \frac{z}{n} \ (n \text{ and } z \text{ are relatively prime }) \tag{2}$$

where, q_1 denotes the number of slot per pole per phase, p denotes the number of pole pairs, s_1 denotes the number of stator slots and m represents the number of phases. If n is even, the

TABLE III
VIBRATION ORDER ACCORDING TO SOURCES

MMF SOURCES	VIBRATION ORDER FREQUENCY	VIBRATION ORDER (K=POSITIVE INTEGER)
Interaction of armature and field	$f_r=(\mu\pm1)f$	$r=p(\mu\pm\nu)$
Interaction of field and stator slotting	$f_r=(\mu_1\pm\mu_2)f$	$r=p(\mu_1\pm\mu_2)\pm ks_1$
Interaction of armature and stator slotting	$f_r=2f$	$r=p(\nu_1+\nu_2)\pm ks_1$
Field	$f_r=(\mu_1\pm\mu_2)f$	$r=p(\mu_1\pm\mu_2)$
Armature	$f_r=2f$	$r=p(\nu_1+\nu_2)$

spatial order is

$$\nu = \pm\frac{1}{n}(2mk+2) \tag{3}$$

if n is odd, the spatial order is

$$\nu = \pm\frac{1}{n}(2mk+1) \tag{4}$$

where k is an integer, such as 0, ±1, ±2, ±3 …. The $\pm$ sign in (3) and (4) is chosen to be + or – to make the equations yield a positive sign for the fundamental ($\nu = +1$). For instance, in a three-phase motor with 8 poles and 12 slots, when $s_1 = 12$, $p = 4$, and $m = 3$, $z = 1$ and $n = 2$. As n is an even number, $\nu = 1$ is satisfied, when it has a positive sign in (3). The order of the spatial harmonics of the field depends on the vibration order frequency of being analyzed. In the case of a PM machine, vibration occurs primarily when it is twice the frequency of the rotating magnetic field, and the corresponding spatial harmonic order occurs by the field [20]. The vibration order according to the MMF sources constituting the spatial harmonics are listed in Table III. In Table III, μ denotes the spatial harmonic order of the MMF caused by field, ν denotes the spatial harmonic order of the MMF caused by armature reaction, r denotes the vibration order, f denotes the fundamental frequency, f_r denotes the vibration order frequency to be analyzed. For all the sources, the absolute lowest value of the vibration order calculated by μ and ν can be regarded as the vibration order of the corresponding pole slots combination. The vibration order of the 8-pole 12-slot motor for each MMF source is 4.

2) Electromagnetic Force Calculation Considering Tooth Modulation Effect: The distributed electromagnetic pressure is obtained from the relationship between the air gap flux density in the radial and tangential directions. According to the Maxwell stress tensor, the radial and tangential electromagnetic force per unit area or electromagnetic pressure waveform at any point in the air gap is expressed in [22]:

$$p_r(\alpha,t) = \frac{1}{2\mu_0}\left[b_r^2(\alpha,t) - b_t^2(\alpha,t)\right] \tag{5}$$

$$p_t(\alpha,t) = \frac{1}{\mu_0} b_r b_t \tag{6}$$

where, p_r and p_t denotes the radial and tangential electromagnetic pressure, b_r denotes the radial flux density of the air gap, b_t corresponds to the tangential flux density of the air gap, μ_0 denotes the magnetic permeability of vacuum, α represents the

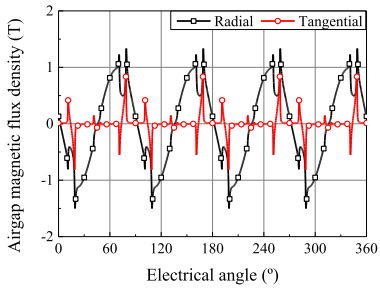

Fig. 11. Radial and tangential magnetic flux density under maximum load condition during normal operation.

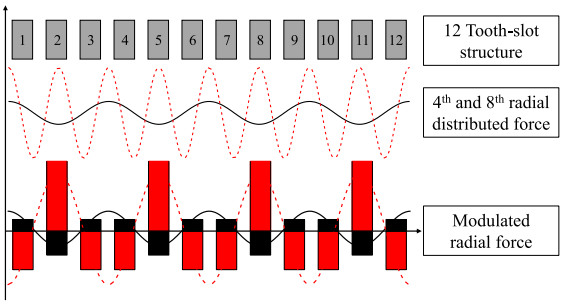

Fig. 12. Process of tooth modulation effect of 4th and 8th vibration order radial force due to the 12 tooth-slot structure.

TABLE IV
ELECTRO-MAGNETIC MODULATED FORCES

SYMMETRY		RADIAL	TANGENTIAL
Normal Operation		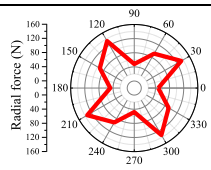	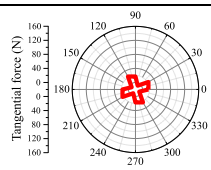
Fault Operation	Line	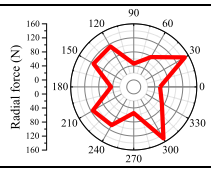	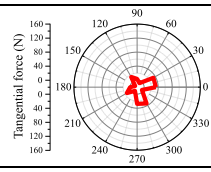
	Point	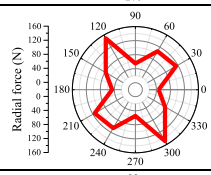	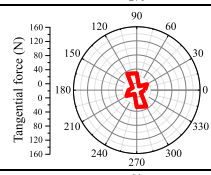
	Alternating	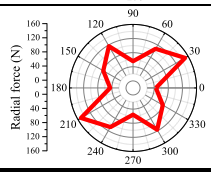	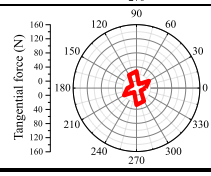

angular distance from the origin of the coordinate system, and t denotes the time. Generally, radial magnetic flux density is much larger than tangential component. Fig. 11 shows the radial and tangential airgap magnetic flux density under maximum load condition during normal operating condition. It can be seen that the radial magnetic flux density is much larger than that of tangential component. This implies that radial electromagnetic force is also much larger than that of the tangential electromagnetic force. The magnetic flux lines are substantially perpendicular to the stator and rotor cores because the permeability of the ferromagnetic core is much higher than that of the air gap [20].

Recently, studies have been conducted that high vibration order electromagnetic force behaves like low vibration order electromagnetic force and causes large vibration, and this effect is called the tooth modulation effect [24]. Fig. 12 shows the tooth modulation process by 12-teeth-slot structure of the 4th and 8th vibration order radial force. As can be seen, 8th vibration order radial force is modulated into 4th vibration order radial force due to 12-teeth-slot structure. Therefore, in this study, concentrated force was calculated instead of distributed force and compared according to the winding arrangement in faulty condition. The concentrated radial and tangential force were calculated as follows [25]:

$$F_{r,z} = \int_{\theta_z-\pi/s+\alpha/2}^{\theta_z+\pi/s-\alpha/2} R_{in} L_{stk} \{p_r \cos(\theta_z-\theta) + p_t \sin(\theta_z-\theta)\} d\theta \tag{7}$$

$$F_{t,z} = \int_{\theta_z-\pi/s+\alpha/2}^{\theta_z+\pi/s-\alpha/2} R_{in} L_{stk} \{p_t \cos(\theta_z-\theta) + p_r \sin(\theta_z-\theta)\} d\theta \tag{8}$$

here, F is the concentrated force, p is the distributed electromagnetic pressure as in (5), (6), L_{stk} is the stack length, θ is the mechanical angle, θ_z is the mechanical angle of the zth tooth center, α is the slot opening angle, subscripts r and t denote radial and tangential directions, respectively, and z is the tooth number.

To calculate the accurate electromagnetic force, a 2D electromagnetic FEA called JMAG was utilized. First, the distributed electromagnetic pressure was calculated according to (5), (6) under the phase current 100 A_{pk}, considering the maximum load condition, and from the calculated pressure, concentrated radial and tangential force were calculated using (7), (8). The calculated radial and tangential concentrated force are shown in Table IV. In Table IV, the red lines in the graphs are a line which is connected the amplitude of the forces at the center point of each tooth. In the case of the maximum load of the target motor, the radial force is approximately four times larger than the tangential force listed in Table IV, based on the electromagnetic force of the maximum value applied to the teeth. As mentioned earlier, this occurs because the radial magnetic flux density is larger than tangential component.

For normal operation, the electromagnetic forces in the four directions were symmetrical, which leads the vibration order of 4. It is primarily because the magnetic flux has a symmetrical shape at intervals of 90°, as shown in Fig. 13(a). For line symmetry, the magnetic flux form is asymmetric as shown in Fig. 13(b), which leads to the vibration order 1 of the electromagnetic forces. For point and alternating symmetry, even though the phase of magnetic flux is different, the magnetic flux has symmetrical shape at intervals of 180°, which leads to the vibration order of 2, as shown in Fig. 13(c) and (d). Using

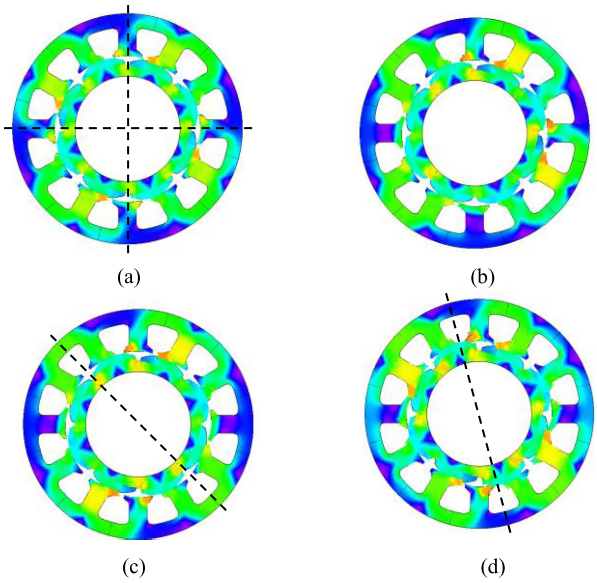

Fig. 13. Flux distribution during normal and fault operation. (a) Normal. (b) Line symmetry during fault. (c) Point symmetry during fault. (d) Alternating symmetry during fault.

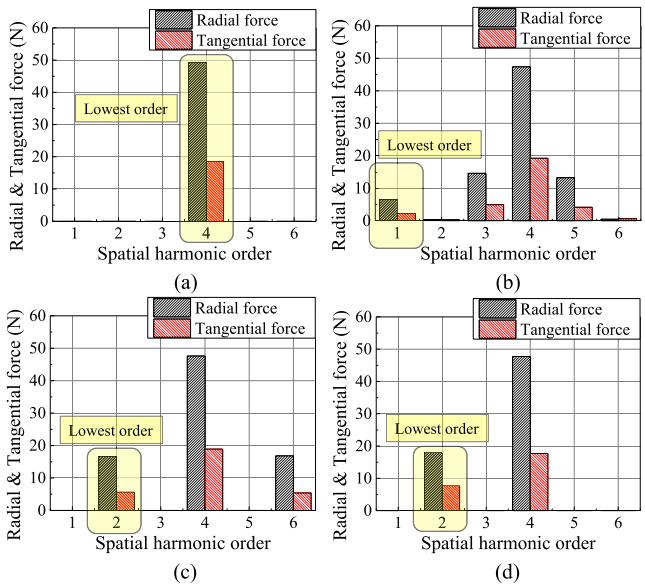

Fig. 14. Amplitude of radial and tangential force. (a) Normal operation. (b) Line symmetry. (c) Point symmetry. (d) Alternating symmetry.

FFT, the amplitude of radial and tangential force is calculated as shown in Fig. 14. Since deformation is an inverse function of fourth power of the vibration order as in (1), as the vibration order decreases, the deformation increases. Therefore, it can be predicted that the deformation of line symmetry is the largest, followed by point and alternating symmetry, and smallest for normal operation.

3) Deformation: The simulation result through JMAG analysis is the same as that in Table V. The figures in Table V were observed by magnifying the deformation size at the same scale. The shape of the force distribution in Table IV and the deformation in Table V are similar. In line symmetry, because

TABLE V
DEFORMATION ANALYSIS RESULT

SYMMETRY	TOP VIEW	LEFT VIEW
Line	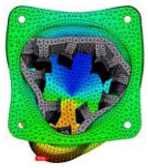	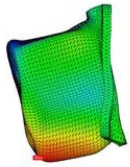
Point	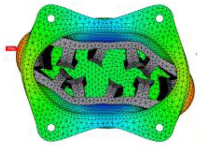	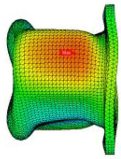
Alternating	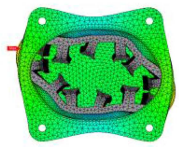	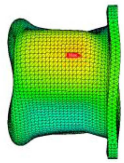

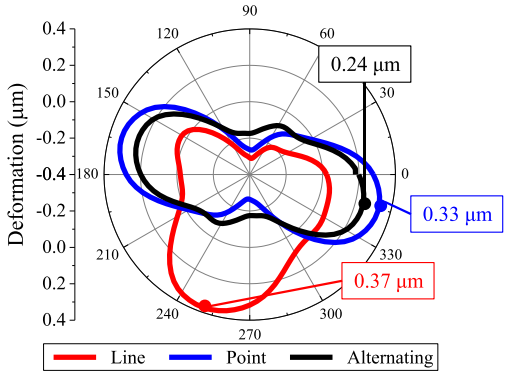

Fig. 15. Amount of deformation around motor housing.

the force in one direction is asymmetrically large, the deformation form is also significantly deformed in one direction. In point and alternating symmetry, the force is symmetrical in two directions, and the deformation also occurs symmetrically in two directions. The amount of deformation according to the winding arrangement around the housing at the point where the maximum deformation occurred is illustrated in Fig. 15. The deformation increases in the order of line > point > alternating symmetry, and it is expected that the noise and vibration are also large in the same order.

The difference in the amount of deformation between the point and the alternating symmetry is considerably large compared to the difference in the amplitude of its force, which is shown in Fig. 14. It caused by the phase difference of forces, which affects deformation [22] between the radial and tangential forces. Fig. 16 shows the radial deformation contributing phase of radial and tangential force, and phase difference of radial and tangential force contributing to radial deformation. Here, since the radial deformation is mostly caused by the lowest vibration order, only the force phase corresponding to the lowest vibration order that can occur according to each winding arrangement is expressed.

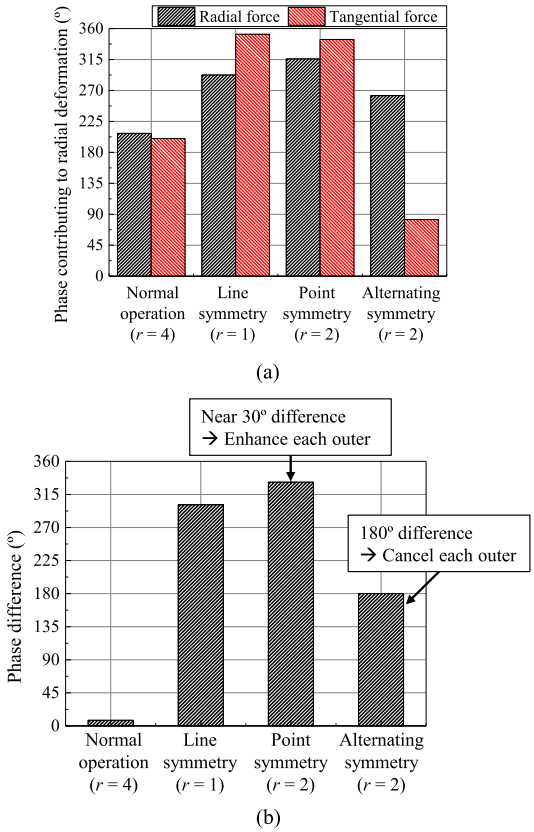

Fig. 16. Phase difference between two forces affecting the deformation. (a) Phase of the radial and tangential forces contributing to radial deformation. (b) Phase difference between the radial and tangential forces.

For point symmetry and alternating symmetry, although the amplitude of radial and tangential force is similar, the phase difference is greatly different. For point symmetry, the phase difference is almost 30°, which means that radial deformation caused by radial force and tangential force enhance each other. On the other hand, for alternating symmetry, the phase difference is almost 180°, which means that radial deformation caused by radial force and tangential force cancel each other out. Therefore, the radial deformation of alternating symmetry is smaller than point symmetry, although amplitude of force is similar. For normal operation, the phase difference is almost zero, and for line symmetry, the phase difference is about 60°. In both operating condition, radial deformation could be enhanced by radial and tangential force.

C. Thermal Characteristics

The differences in thermal characteristics according to winding arrangement during fault operation in transient and steady state is analyzed through simulation results of a lumped parameter thermal network with piecewise stator-housing modules (LPTN with PSMs) and test results.

1) Basic Theory of LPTN With PSM: Based on the winding arrangement, the temperature of the coil hot spot may different during fault operation. LPTN with PSMs which is capable of accurate temperature estimation during fault operation is used to predict the temperature during fault operation in a dual-winding motor [23]. Fig. 17 illustrates the heat transfer path according to the operating mode. Fig. 17(a) depicts the heat transfer path during the fault operation. When one of the two circuits of the motor fails, the current flows in only one circuit, which increases the coil temperature of one circuit due to copper loss. Meanwhile, since current does not flow in the other coil, copper loss does not occur in it; thus, its coil temperature is low. Therefore, heat is transferred in the radial and tangential directions together, as indicated by the yellow arrow in Fig. 17(a), when heat is transmitted from high to low temperature. Fig. 17(b) illustrates the heat transfer path during normal operation. Ideally, the same current flows through all coils, resulting in equal copper loss; thus, all coils have the same temperature. Therefore, heat is transferred only in the radial direction.

Fig. 17. Heat-transfer path according to operation. (a) Fault operation. (b) Normal operation.

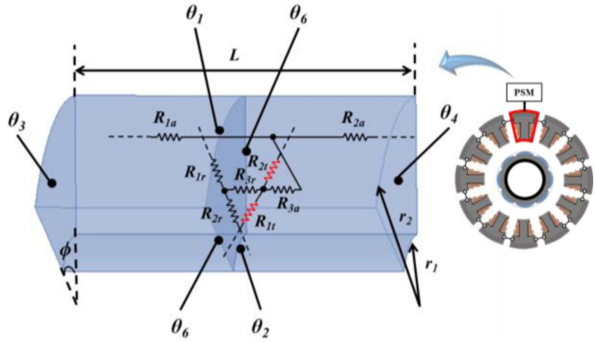

Fig. 18. Diagram of 1/*n* model of the cylindrical component in the PSM.

Fig. 18 depicts the partial model of the entire cylinder divided by *n* slots which is the fundamental model of a PSM. The red resistors in Fig. 18 are the thermal resistances for heat transfer to the left and right in the case of a temperature difference for each of the *n* models. The thermal network of PSM is presented in Fig. 19. The geometric mean distance was used to calculate the left and right thermal resistances. The general resistance equation of the 1/*n* cylindrical component model is as follows:

$$R_{1a} = \frac{360L}{2\pi k_{la}\left(r_1^2 - r_2^2\right)} \tag{9}$$

$$R_{2a} = \frac{360L}{2\pi k_{la}\left(r_1^2 - r_2^2\right)} \tag{10}$$

$$R_{3a} = \frac{-360L}{6\pi k_{la}\left(r_1^2 - r_2^2\right)\phi} \tag{11}$$

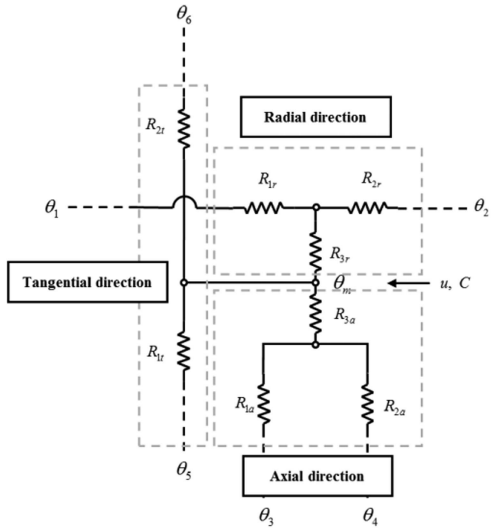

Fig. 19. Thermal network of PSM.

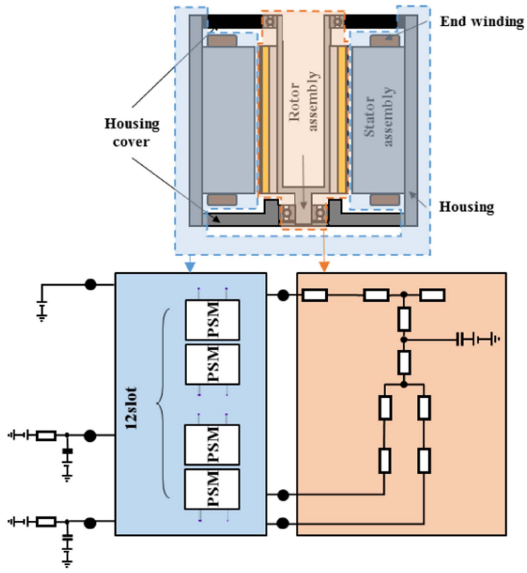

Fig. 20. LPTN using PSM of test motor.

$$R_{1r} = \frac{360}{4\pi k_{lr} L\phi}\left[1 - \frac{2r_2^2 \ln\left(\frac{r_1}{r_2}\right)}{\left(r_1^2 - r_2^2\right)}\right] \tag{12}$$

$$R_{2r} = \frac{360}{4\pi k_{lr} L\phi}\left[\frac{2r_1^2 \ln\left(\frac{r_1}{r_2}\right)}{\left(r_1^2 - r_2^2\right)} - 1\right] \tag{13}$$

$$R_{3r} = \frac{-360}{8\pi\left(r_1^2 - r_2^2\right) k_{lr} L\phi}\left[r_1^2 + r_2^2 - \frac{4r_1^2 r_2^2 \ln\left(\frac{r_1}{r_2}\right)}{\left(r_1^2 - r_2^2\right)}\right] \tag{14}$$

$$R_{1t} = \frac{\pi \cdot \phi \cdot e^{\frac{r_1^2 \ln r_1 - r_2^2 \ln r_2}{r_1^2 - r_2^2} - \frac{1}{2}}}{k_{lr} \cdot s \cdot L \cdot (r_1 - r_2) \cdot 360} \tag{15}$$

$$R_{2t} = \frac{\pi \cdot \phi \cdot e^{\frac{r_1^2 \ln r_1 - r_2^2 \ln r_2}{r_1^2 - r_2^2}}}{k_{lr} \cdot s \cdot L \cdot (r_1 - r_2) \cdot 360} \tag{16}$$

$$C = \frac{c\rho\pi L s\left(r_1^2 - r_2^2\right)\phi}{360} \tag{17}$$

As shown in Fig. 20, the temperature of the dual-winding motor according to the winding arrangement is calculated using LPTN with PSMs.

2) Result of Temperature According to Winding Arrangement: To measure the temperature according to the winding arrangement using one sample, as shown in the expanded view of the test motor in Fig. 21, female terminals were connected to each coil of the 12 slots so that the coils of each slot could be connected. The electrical circuits were connected according to the winding arrangement shown in Fig. 7 to classify working and non-working slots. Working slots are colored in bright red and non-working slots are colored in bright blue. Six cases were compared according to the winding arrangement (three cases: line, point, alternating symmetry) in the dual-winding motor and the current value (two cases: 20 and 100 A_{pk}) during fault operation in which heat transfer occurs in the tangential direction.

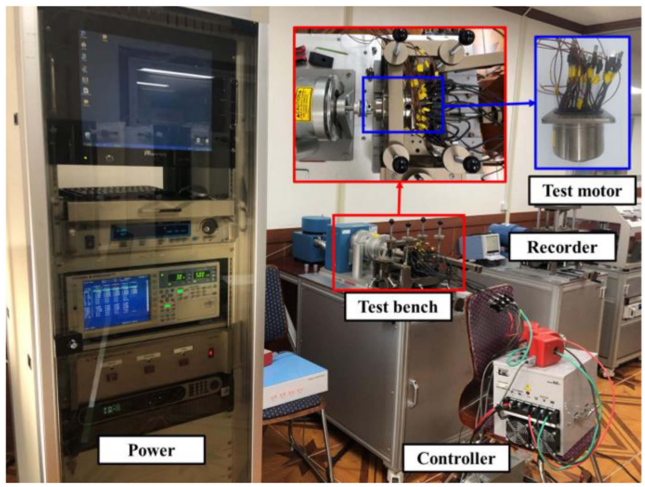

Fig. 21. Test environment.

Simulation and test results at 20 A_{pk} and 100 A_{pk} currents were compared to confirm the transient and steady-state conditions. Based on the winding arrangement of the dual-winding motor, the coils that should have the same temperature under ideal conditions were grouped together. During the simulation, the coils in each group had the same temperature. For coils in working slots, for example, in the line symmetry case, the temperatures of the coils (3, 4), (2, 5), (1, 6) in Fig. 7(a) are grouped. In the point symmetry case, the temperatures of coils (3, 9) and (2, 4, 8, 10) in Fig. 7(b) are grouped. In the alternating symmetry case, the temperatures of the coils (1, 3, 5, 7, 9, 11) in Fig. 7(c) are grouped.

Fig. 22 illustrates the simulation and test results of the coil temperature based on the winding arrangement at 20 and 100 A_{pk} currents during fault operation. Because the measured coil temperature exhibits a difference within 5-10°C within each group, the average temperature of each group was used to compare with the simulation results. The test and simulation

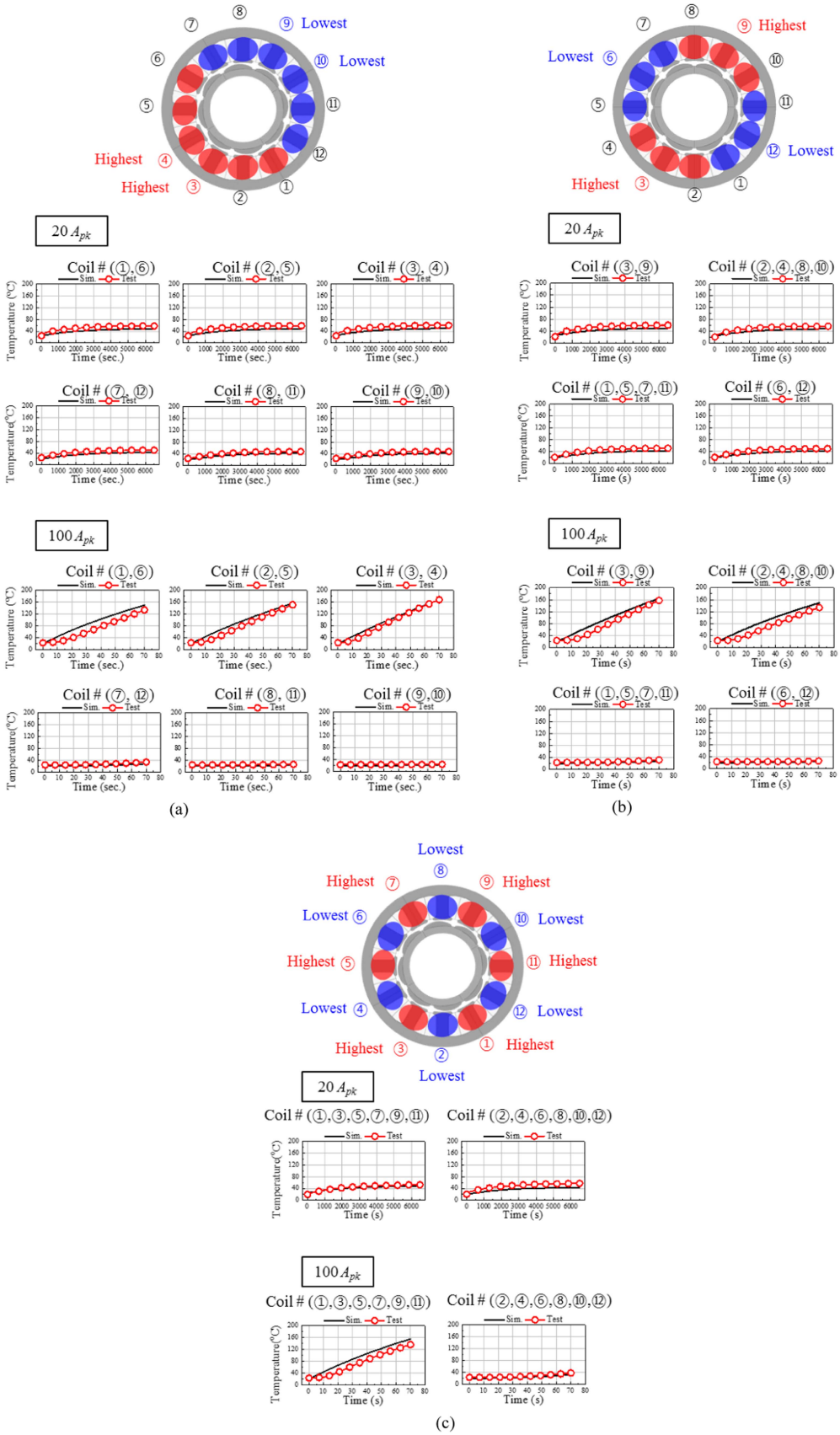

Fig. 22. Simulation and test result of temperature during fault operation. (b) Point symmetry. (c) Alternating symmetry.

TABLE VI
TEMPERATURE DATA DURING FAULT OPERATION

(a)

COIL NO.	ITEM	CURRENT: 20 A_{PK}	CURRENT: 100 A_{PK}
①,⑥	Simulation (℃)	48.1	150.2
	Test (℃)	57.6	134.3
	Error (℃)	9.5	-15.9
②,⑤	Simulation (℃)	48.6	156.1
	Test (℃)	58.8	151.5
	Error (℃)	10	-4.6
③,④	Simulation (℃)	49.6	168.2
	Test (℃)	59.7	168.6
	Error (℃)	10	0.4
⑦,⑫	Simulation (℃)	42.6	27.1
	Test (℃)	49.5	33.2
	Error (℃)	6.9	6.1
⑧,⑪	Simulation (℃)	42.1	22.8
	Test (℃)	47.5	25.2
	Error (℃)	5.4	2.35
⑨,⑩	Simulation (℃)	42	22.6
	Test (℃)	47.8	24.5
	Error (℃)	5.8	1.9

(b)

COIL NO.	ITEM	CURRENT: 20 A_{PK}	CURRENT: 100 A_{PK}
③,⑨	Simulation (℃)	49.3	164.1
	Test (℃)	59.4	157.3
	Error (℃)	10.1	-6.8
②,④, ⑧,⑩	Simulation (℃)	48.1	149.1
	Test (℃)	57.3	133.6
	Error (℃)	9.2	-15.5
①,⑤, ⑦,⑪	Simulation (℃)	42.6	27.5
	Test (℃)	51.3	31.7
	Error (℃)	8.7	4.2
⑥,⑫	Simulation (℃)	42.2	23.1
	Test (℃)	50	25.5
	Error (℃)	7.8	2.4

(c)

COIL NO.	ITEM	CURRENT: 20 A_{PK}	CURRENT: 100 A_{PK}
①,③,⑤, ⑦,⑨,⑪	Simulation (℃)	48.4	155.6
	Test (℃)	57.2	139.5
	Error (℃)	8.8	-16.1
②,④,⑥, ⑧,⑩,⑫	Simulation (℃)	43.1	32.7
	Test (℃)	52.6	38.8
	Error (℃)	9.5	6.1

results are compared according to the winding arrangement, coil position and current. In the graphs, the red solid line with white dots represents the test result, and the black solid line represents the simulation result. The final temperature and error of the simulation and test for the same period are recorded in Table VI. It can be seen that the simulation and test temperatures were almost identical. When a steady state 20 A_{pk} current was applied, the highest temperature among the test and simulation results was in the order of line > point > alternating symmetry, and the lowest temperature was in the order of line < point < alternating symmetry. However, depending on the winding arrangement and position of the coil, the temperatures were at the same level. In the case of a transient state in which 100 A_{pk} current was applied, the temperature difference between the coils was large depending on the position of the coils within the same operating time; however, the order of the highest and lowest temperatures according to the winding arrangement was the same as when a 20 A_{pk} current was applied.

Heat transfer primarily occurs through conduction inside the motor, and a time delay occurs owing to the heat capacity of each component constituting the PSM until the heat generated from the working PSM is transferred to the non-working PSM. As shown in Fig. 22, in the line symmetry result when a current of 20 A_{pk} was applied, the temperature of each coil position is similar regardless of the winding arrangement. This is because there was sufficient time for the heat to transfer to each adjacent PSM before the coil temperature reached its usage limit. However, in the transient state in which the 100 A_{pk} current was applied, the gap between the maximum and the minimum temperatures was considerably larger because the coil temperature of the working PSM reached the limit of use within a short time period, so there was not insufficient time for the heat generated in the working PSM to be transferred to the non-working PSM.

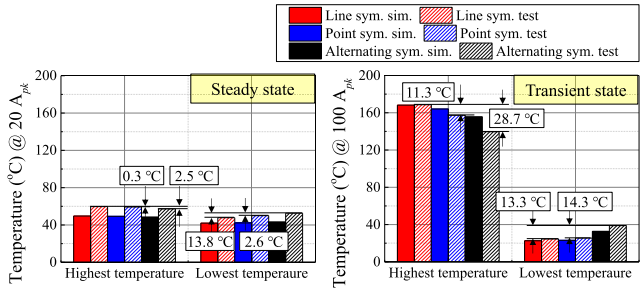

Fig. 23. Temperature difference in steady and transient state.

The above test results only discussed the steady state of low current and the transient state of high current when a constant current was applied. However, if the input and non-input of the motor current are repeated during brake operation and non-operation, the coil temperature difference accumulates, resulting in a larger temperature difference for each winding arrangement as shown in Fig. 23. Therefore, heat transfer of alternating symmetry occurs relatively actively compared to point or line symmetry. Hence, it is most advantageous in terms of thermal characteristics, whereas line symmetry is disadvantageous in terms of thermal characteristics because the heat transfer of the coil hot spot is sluggish.

D. Mechanical Characteristics

In this analysis, only parts of the stator assembly and housing were considered, although the length of the shaft also changes according to the winding arrangement. The parts of the stator assembly were bus-bars and insulators. As the number of bus-bars increases according to the winding arrangement, the height of the molding part including the bus-bars increases, and the number of insulator guides increases. Consequently, it leads to an increase in the size of the insulator, which also increases the size of the housing including the insulator and bus-bars. As shown in Fig. 7, the bus-bar in the motor connects to each phase. Fig. 7 illustrates the bus-bar connection according to the winding arrangement of the 8-pole 12-slot concentrated winding model. The primary and secondary circuits are separated from each other, and each phase consists of two series circuits for each circuit. A connected core method is applied to the stator of the target motor; thus, the same phases are connected without a bus-bar, and the different phases are connected to a bus-bar, as shown in Fig. 7. When designing a bus-bar, it is crucial to consider the insulation distance to satisfy the international standard IEC 60664-1. Securing the insulation distance is a

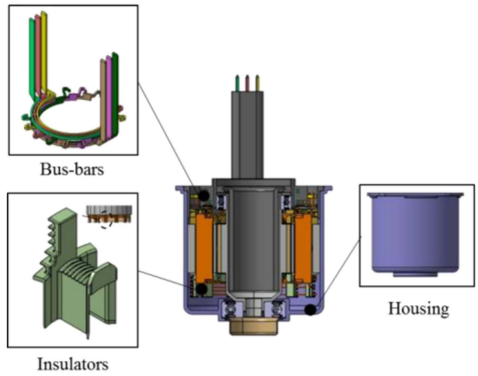

Fig. 24. Design changed parts.

requirement to satisfy the test standards for withstanding voltage and insulation resistance. In addition, the design should also consider manufacturing methods. To maintain the separation distance between the bus-bars due to vibration and shock during operation, the bus-bars are molded together by plastic molding. In this paper, the distance between the bus-bars is designed to be more than 1.0 mm when designing the bus-bars, primarily in consideration of the thermal flowability of the injection-molded material, deformation and change in the position of the bus-bars due to the injection pressure.

When the coils between the slots are connected in a series circuit, a guide is necessary to prevent any interference between the wires of different phases. If there is no guide, it is difficult to make the resistance of the three-phase uniform during manufacturing, and the insulation may be broken by the interference between the wires of different phases due to the vibration during motor operation, which may cause a short circuit between the coils. The box marked with the dotted line in Fig. 7 indicates that a wire guide is required. This role is primarily implemented in the shape of the insulator, and the number of guides of the insulator is determined according to the number of overlapping wires. In case of line symmetry, a maximum of three wires overlap between coils 3 and 4 and between coils 9 and 10; in the case of point symmetry, a maximum of six wires overlap between coils 7 and 8. Lastly, in the case of alternating symmetry, a maximum of six wires overlap between coils 6 and 7. In line symmetry, bus-bars are designed with one layer; in point and alternating symmetry, the bus-bars are composed of two layers designed to satisfy the design criteria mentioned above.

The bus-bars which are changed from one layer to two layers and insulators which is changed from three wire guides to six wire guides make the size increment of the motor housing. Fig. 24 illustrates the parts that should be designed and Table VII lists the changed design features. Compared to line symmetry, the size increased by 10.4 mm in point and alternating symmetry. The increased size inflicts a price increase of $0.21 and $0.24, respectively in point symmetry and alternating symmetry when compared with the line symmetry.

E. Overall Performance Comparison

In Tables VIII and IX, the characteristics of dual-winding motor during the fault operation are summarized quantitatively and qualitatively, respectively. Evidently, line symmetry is the best in terms of size and price, and the point and alternating symmetry are similar. However, in alternating and point symmetry, the thermal, noise, and vibration properties are superior to the line symmetry. In the steady state, the temperature characteristics are the same for the three winding arrangements at the same current. In the transient state, the thermal characteristics are superior in the order of alternating symmetry and line symmetry. Line symmetry is most vulnerable to noise and vibration because the vibration order is 1, and alternating symmetry is the best. The alternating symmetry based on the same torque has the smallest input current and is the best in terms of torque; however, the difference is not significant. The order of the torque ripple amplitude of the point and line symmetry is reversed depending

TABLE VII
MECHANICAL DESIGN FEATURE

	LINE	POINT	ALTERNATING
Bus-bars	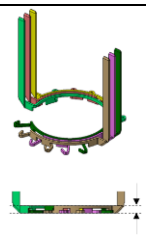	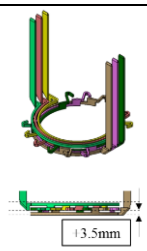	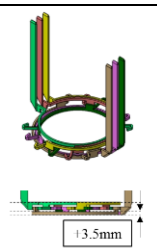
Insulators	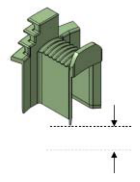	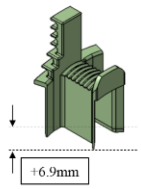	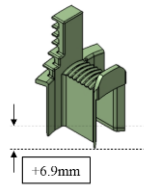
Housing		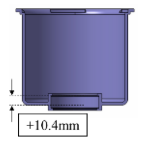	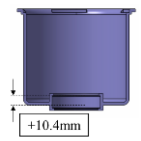
Section	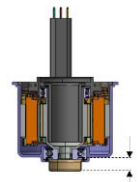	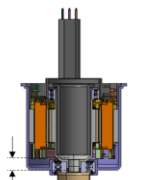	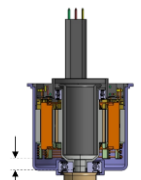

TABLE VIII
MOTOR PERFORMANCE ACCORDING TO WINDING ARRANGEMENT

CHARACTERISTIC		LINE	POINT	ALTERNATING
Size (mm)		0 (base)	+10.4	+10.4
Cost ($)		0 (base)	+0.21	+0.24
Maximum temperature (°C)	Transient	59.7	59.4	57.2
	Steady	168.6	157.3	139.5
Maximum deformation (μm)		0.37	0.33	0.24
Torque ripple (%)		5.77	5.11	3.63
Phase current for same output torque (A_{pk})		103.0	102.5	102.2

TABLE IX
OVERALL ASSESSMENT ACCORDING TO WINDING ARRANGEMENT

CHARACTERISTIC		LINE	POINT	ALTERNATING
Size		◎	△	△
Cost		◎	△	△
Thermal	Transient	△	○	◎
	Steady	○	○	○
Noise & Vibration		△	○	◎
Torque		○	○	○

on the order; however, alternating symmetry is the best in the entire range of torque ripple.

IV. CONCLUSION

In this study, the multi-physics characteristics of a dual-winding motor for IEB redundancy according to the winding arrangement were compared during fault operation. First, torque and torque ripple that can represent electrical characteristics were compared. Second, electromagnetic force and vibration characteristics were analyzed and compared considering tooth modulation effect. Third, the thermal characteristics were compared through tests and simulations. Fourth, a dual-winding motor was described from a mechanical design and price perspectives. All of these characteristics were investigated and compared according to the winding arrangement, and it was confirmed that multi-physics performance is greatly affected by winding arrangement in a faulty condition. This study is a useful reference when determining the winding arrangement in a system using dual-winding motors to prepare for fault operation, because the overall performance of the motor is all compared through this study. Although this study is limited to an 8-pole 12-slot motor, characteristics for other poles/slot numbers can be inferred based on the magnetic field distribution and coil arrangement. Even for other motors with different pole and slot combinations, flux distribution under fault operation is determined within line, point, and alternating symmetry. The symmetric type (line, point, and alternating) can be known through the flux distribution, and the symmetric type follows the three types as mentioned.

It is essential to select a winding arrangement that is advantageous for the system. In summary, it is appropriate to select line symmetry for mass-production systems that are greatly affected by price, which can be repaired as soon as possible in case of failure. Meanwhile, alternating symmetry is more suitable for systems that require durability to enable continuous system operation even in the event of a failure. Lastly, point symmetry has no major advantages; therefore, it should be carefully considered when selecting the winding arrangement.

REFERENCES

[1] C. Jeong, J. Park, and N. Bianchi, "Analysis of dual three-phase synchronous reluctance motor by winding function theory," in *Proc. IEEE Int. Conf. Elect. Mach.*, 2020, pp. 2055–2061.

[2] X. Cui, J. Sun, and C. Gu, "Comparative study of performance for different winding connections of dual-channel switched reluctance machine using frozen permeability," in *Proc. IEEE 4th Southern Power Electron. Conf.*, 2018, pp. 1–6.

[3] H. Chen, X. Liu, J. Zhao, and N. A. O. Demerdash, "Magnetic-coupling characteristics investigation of a dual-rotor fault-tolerant PMSM," *IEEE Trans. Energy Convers.*, vol. 33, no. 1, pp. 362–372, Mar. 2018.

[4] E. Mese, M. Tezcan, M. Ayaz, Y. Yasa, and K. Yilmaz, "Design considerations for dual winding permanent magnet synchronous machines," in *Proc. IEEE Energy Convers. Congr. Expo.*, 2012, pp. 1894–1901.

[5] T. Shigeta, K. Akatsu, and T. Kato, "The interior PM application and dual winding method of compound magnet motive forces motor," in *Proc. IEEE Int. Conf. Elect. Mach. Syst.*, 2011, pp. 1–6.

[6] C. Babetto and N. Bianchi, "Synchronous reluctance motor with dual three-phase winding for fault- tolerant applications," in *Proc. IEEE 13th Int. Conf. Elect. Mach.*, 2018, pp. 2297–2303.

[7] W. Zhao, L. Xu, and G. Liu, "Overview of permanent-magnet fault-tolerant machines: Topology and design," *Counselor Educ. Supervision Trans. Elect. Mach. Syst.*, vol. 2, no. 1, pp. 51–64, Mar. 2018.

[8] A. M. EL-Refaie, "Fault-tolerant PM machines: A review," in *Proc. IEEE Int. Electric Mach. Drives Conf.*, 2009, pp. 1700–1709.

[9] Y. Demir and M. Aydin, "A novel asymmetric and unconventional stator winding configuration and placement for a dual three-phase surface PM motor," *IEEE Trans. Magn.*, vol. 53, no. 11, Nov. 2017, Art. no. 8111805.

[10] N. Bianchi, M. D. Pre, and S. Bolognani, "Design of a fault-tolerant IPM motor for electric power steering," *IEEE Trans. Veh. Technol.*, vol. 55, no. 4, pp. 1102–1111, Jul. 2006.

[11] M. Barcaro, N. Bianchi, and F. Magnussen, "Analysis and tests of a dual three-phase 12-slot 10-pole permanent-magnet motor," *IEEE Trans. Ind. Appl.*, vol. 46, no. 6, pp. 2355–2362, Nov./Dec. 2010.

[12] M. Barcaro, L. Alberti, and N. Bianchi, "Thermal analysis of dual three-phase machines under faulty operations," in *Proc. IEEE 8th Symp. Diagn. Elect. Mach., Power Electron. Drives*, 2011, pp. 165–171.

[13] M. Chowdhury, A. Singh, R. Ramakrishnan, M. Islam, and A. Gebregergis, "Performance analysis of dual wound permanent magnet synchronous machines under winding fault scenarios," in *Proc. IEEE Energy Convers. Congr. Expo.*, 2018, pp. 693–700.

[14] P. S. Sangha and T. Sawata, "Design and test results for dual-lane fault-tolerant PM motor for safety critical aircraft actuator," in *Proc. IEEE Energy Convers. Congr. Expo.*, 2015, pp. 4055–4060.

[15] J. Xu, Y. Yuan, Z. Zhang, and H. Guo, "The influence analysis of different fault modes on the post-fault performance of fault tolerant permanent magnet synchronous motor," in *Proc. IEEE 20th Int. Conf. Elect. Mach. Syst.*, 2017, pp. 1–5.

[16] Y. Zhao, H. Wang, D. Li, and R. Qian, "Fault-tolerant performance of a three-phase dual armature-winding doubly salient brushless DC generator," *IEEE Access*, vol. 6, pp. 18022–18031, 2018.

[17] P. Giangrande, V. Madonna, S. Nuzzo, C. Gerada, and M. Galea, "Braking torque compensation strategy and thermal behavior of a dual three-phase winding PMSM during short-circuit fault," in *Proc. IEEE Int. Elect. Mach. Drives Conf.*, 2019, pp. 2245–2250.

[18] S. J. Nall and P. H. Mellor, "A compact direct-drive permanent magnet motor for a UAV rotorcraft with improved faulted behaviour through operation as four separate three-phase machines," in *Proc. 4th Inst. Eng. Technol. Conf. Power Electron., Mach. Drives*, 2008, pp. 245–249.

[19] D.-Y. Kim, M.-R. Park, J.-H. Sim, and J.-P. Hong, "Advanced method of selecting number of poles and slots for low-frequency vibration reduction of traction motor for elevator," *IEEE/Amer. Soc. Mech. Eng. Trans. Mechatronics*, vol. 22, no. 4, pp. 1554–1562, Aug. 2017.

[20] D. A. Crolla, *Automotive Engineering: powertrain, Chassis System and Vehicle Body*. Oxford, U.K.: Butterworth-Heinemann, 2009.

[21] J. F. Geiras, C. Wang, and J. C. Lai, *Noise of Polyphaser Electric Motors*. Boca Raton, FL, USA: CRC Press, 2018.

[22] Y. S. Chen, Z. Q. Zhu, and D. Howe, "Vibration of PM brushless machines having a fractional number of slots per pole," *IEEE Trans. Magn.*, vol. 42, no. 10, pp. 3395–3397, Oct. 2006.

[23] B.-K. Song, J.-W. Chin, D.-M. Kim, K.-Y. Hwang, and M.-S. Lim, "Temperature estimation using lumped-parameter thermal network with piecewise stator-housing modules for fault-tolerant brake systems in highly automated driving vehicles," *IEEE Trans. Intell. Transp. Syst.*, vol. 22, no. 9, pp. 5819–5832, Sep. 2021, doi: 10.1109/TITS.2021.3091621.

[24] H. Fang, D. Li, R. Qu, and P. Yan, "Modulation effect of slotted structure on vibration response in electrical machines," *IEEE Trans. Ind. Electron.*, vol. 66, no. 4, pp. 2998–3007, Apr. 2019.

[25] J.-H. Kim, S.-H. Park, J.-Y. Ryu, and M.-S. Lim, "Comparative study of vibration on 10-pole 12-slot and 14-pole 12-slot PMSM considering tooth modulation effect," *IEEE Trans. Ind. Electron.*, vol. 70, no. 4, pp. 4007–4017, Apr. 2023.

Baik-Kee Song received the B.S. degree in mechanical engineering and the M.S. degree in automotive engineering in 2009 and 2011, respectively, from Hanyang University, Seoul, South Korea, where he is currently working toward the Ph.D. degree in automotive engineering. Since 2011, he has been a Research Engineer in Mando, Seongnam, South Korea.

His research interests include electro-magnetic design of motor and motor thermal analysis using equivalent circuit.

Jae-Hyun Kim received the bachelor's degree in mechanical engineering in 2017 from Hanyang University, Seoul, South Korea, where he is currently working toward the Ph.D. degree in automotive engineering.

His research interests include the design, and analysis of vibration and noise of electric machines.

Kyu-yun Hwang (Member, IEEE) received the B.S. degree in electronic and computer engineering and the Ph.D. degree in electronic, electrical, control, and instrumentation engineering from Hanyang University, Ansan, South Korea, in 2003 and 2021, respectively.

From 2010 to 2012, he was a Research Engineer with Komotek Company Ltd., Seongnam, South Korea. From 2012 to 2022, he was a Senior Engineer with Mando, Seongnam. Since 2022, he has been an Assistant Professor with the School of Railway Operation and Control, Dongyang University, Yeongju, South Korea.

His research interests include design, analysis, and optimization of electric machines.

Myung-Seop Lim received the bachelor's degree in mechanical engineering and the master's and Ph.D. degrees in automotive engineering from Hanyang University, Seoul, South Korea, in 2012, 2014, and 2017, respectively.

From 2017 to 2018, he was a Research Engineer with Hyundai Mobis, Yongin, South Korea. From 2018 to 2019, he was an Assistance Professor with Yeungnam University, Daegu, South Korea. Since 2019, he has been with Hanyang University, Seoul, South Korea, where he is currently an Assistant Professor.

His research interests include electromagnetic field analysis and multiphysics analysis of electric machinery for mechatronics systems, such as automotive and robot applications.